

Free-electron lasing with compact beam-driven plasma wakefield accelerator

<https://doi.org/10.1038/s41586-022-04589-1>

Received: 11 June 2021

Accepted: 25 February 2022

Published online: 25 May 2022

 Check for updates

R. Pompili¹✉, D. Alesini¹, M. P. Anania¹, S. Arjmand¹, M. Behtouei¹, M. Bellaveglia¹, A. Biagioni¹, B. Buonomo¹, F. Cardelli¹, M. Carpanese², E. Chiadroni¹, A. Cianchi^{3,4,5}, G. Costa¹, A. Del Dotto¹, M. Del Giorno¹, F. Dipace¹, A. Doria², F. Filippi², M. Galletti^{3,4,5}, L. Giannessi¹, A. Giribono¹, P. Iovine⁶, V. Lollo¹, A. Mostacci⁷, F. Nguyen², M. Opronella⁸, E. Di Palma², L. Pellegrino¹, A. Petralia², V. Petrillo⁸, L. Piersanti¹, G. Di Pirro¹, S. Romeo¹, A. R. Rossi⁸, J. Scifo¹, A. Selce², V. Shpakov¹, A. Stella¹, C. Vaccarezza¹, F. Villa¹, A. Zigler^{1,9} & M. Ferrario¹

The possibility to accelerate electron beams to ultra-relativistic velocities over short distances by using plasma-based technology holds the potential for a revolution in the field of particle accelerators^{1–4}. The compact nature of plasma-based accelerators would allow the realization of table-top machines capable of driving a free-electron laser (FEL)⁵, a formidable tool to investigate matter at the sub-atomic level by generating coherent light pulses with sub-ångström wavelengths and sub-femtosecond durations^{6,7}. So far, however, the high-energy electron beams required to operate FELs had to be obtained through the use of conventional large-size radio-frequency (RF) accelerators, bound to a sizeable footprint as a result of their limited accelerating fields. Here we report the experimental evidence of FEL lasing by a compact (3-cm) particle-beam-driven plasma accelerator. The accelerated beams are completely characterized in the six-dimensional phase space and have high quality, comparable with state-of-the-art accelerators⁸. This allowed the observation of narrow-band amplified radiation in the infrared range with typical exponential growth of its intensity over six consecutive undulators. This proof-of-principle experiment represents a fundamental milestone in the use of plasma-based accelerators, contributing to the development of next-generation compact facilities for user-oriented applications⁹.

Particle accelerators have been one of the key engines for new advancements in physics, giving researchers a valuable tool to investigate matter with atomic and sub-atomic resolution. Their implementation in fourth-generation light sources based on FELs, for instance, allowed the generation of coherent light pulses that can even reach the hard X-rays range at the attosecond timescale by using electron beams with tens of GeV energies^{6,7}. However, the underlying accelerator technology that makes use of RF waves has mostly remained unchanged over the decades. Achieving such large energies required therefore the realization of machines with large sizes and prohibitive costs, mostly owing to the limited accelerating fields provided by RF technology¹⁰.

Such a limitation has stimulated a rapidly growing research area exploiting the huge electric fields generated in a plasma¹¹ and paving the way towards the development of futuristic compact machines, such as EuPRAXIA⁹. Tremendous progress was achieved with pioneering experiments driven by high-intensity laser pulses^{12,13} or ultra-relativistic particle beams^{3,14} that demonstrated accelerations up to hundreds of GV m⁻¹, that is orders of magnitude larger than current RF technology. However, despite such large gradients and following advances to improve the resulting beam quality^{15–18}, the first lasing of a FEL was

demonstrated only very recently adopting a laser-driven wakefield accelerator¹⁹.

Here we present the first proof-of-principle experiment demonstrating self-amplified spontaneous emission (SASE) in a FEL from a centimetre-scale beam-driven plasma wakefield accelerator (PWFA)²⁰. The experiment is performed at the SPARC_LAB test facility²¹, where the accelerating field, generated in the plasma by a relativistic particle bunch acting as driver, is used to accelerate a trailing witness bunch. The witness gains about 6 MeV energy over a 3-cm-long plasma, has low energy spread ($\sim 0.3\%$) and emittance (a few microns) and is highly stable and reproducible. The six-dimensional phase space of the accelerated beam is completely characterized and matched into the FEL beamline to drive light amplification. Here we observed the spectrum and exponential growth of the amplified light along six planar undulators, confirming the typical features of SASE.

The experimental setup is shown in Fig. 1. Two ultra-short driver and witness electron bunches are generated by the SPARC_LAB photo-injector, consisting of a RF gun followed by three accelerating sections. The bunches come from the photoemission of a copper cathode illuminated by two ultraviolet pulses²² and are compressed

¹Laboratori Nazionali di Frascati, Frascati, Italy. ²ENEA Fusion and Technology for Nuclear Safety and Security Department (FSN), C.R. Frascati, Frascati, Italy. ³University of Rome Tor Vergata, Rome, Italy. ⁴INFN Tor Vergata, Rome, Italy. ⁵NAST Center, Rome, Italy. ⁶INFN Napoli, Naples, Italy. ⁷Sapienza University, Rome, Italy. ⁸INFN Milano, Milan, Italy. ⁹Racah Institute of Physics, Hebrew University, Jerusalem, Israel. ✉e-mail: riccardo.pompili@lnf.infn.it

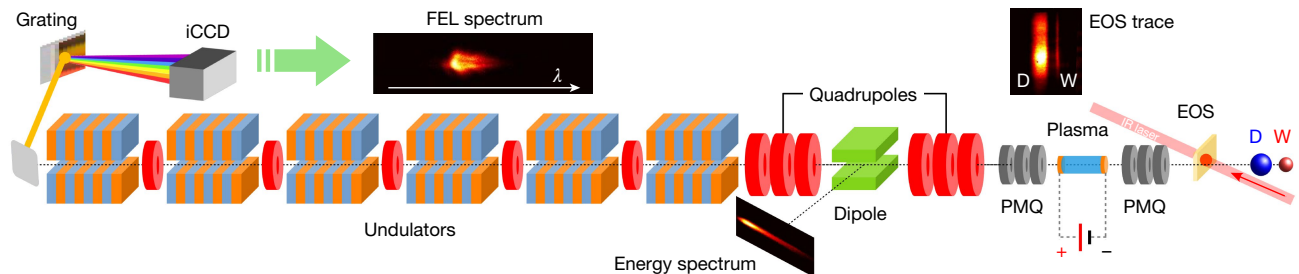


Fig. 1 | Experimental setup. The driver (D) and witness (W) electron bunches are produced by the photo-injector and their temporal separation is continuously monitored with a non-intercepting EOS diagnostics. The bunches are focused by a triplet of PMQs in a 3-cm-long capillary containing the plasma produced by ionizing hydrogen gas with a high-voltage discharge. The accelerated witness is extracted by a second triplet of PMQs and transported using six electromagnetic quadrupoles. A dipole spectrometer is used to

measure its energy with a scintillator screen installed on a 14° beamline. The FEL beamline consists of six planar undulators with tunable gaps and five quadrupoles in between to transport the beam. The emitted FEL radiation is collected by an in-vacuum metallic mirror and measured with an imaging spectrometer equipped with a diffraction grating and a cooled intensified camera (iCCD).

down to durations of a few tens of femtoseconds by tuning the first accelerating section at close-to-zero phase²³. The beam diagnostics upstream of the plasma module consists of a non-intercepting and single-shot electro-optical sampling (EOS) that continuously monitors the bunch durations and separation²⁴. Downstream of the plasma, a RF deflector and a magnetic spectrometer allow to characterize the time and energy profiles of the beam, in correspondence of a cerium-doped yttrium aluminium garnet (Ce:YAG) screen²⁵.

The plasma accelerator module consists of a 3D-printed capillary with length $L_p = 3$ cm and a diameter of 2 mm. The capillary is filled with hydrogen gas through two symmetric inlets. The plasma is generated by ionizing the gas with a high-voltage discharge providing 5-kV pulses with a current of 120 A and duration $\approx 1 \mu\text{s}$. The stability and repeatability of the plasma formation is obtained by pre-ionizing the gas with a Nd:YAG laser focused at the capillary entrance. This reduces the discharge timing jitter from tens to a few nanoseconds and, in turn, the plasma density fluctuations from 12% to 6% (ref. ²⁶). Two triplets of movable permanent-magnet quadrupoles (PMQs) are installed upstream and downstream of the capillary to focus the beam into the plasma and extract from it after acceleration²⁷.

The FEL beamline consists of six undulators, each one of length 2.15 m with 77 periods, with each period $\lambda_u = 2.8$ cm. A quadrupole is installed between two consecutive undulators to transport the beam. The gap of each undulator can be tuned to adjust the undulator parameter in the range $K_u \approx 0.4\text{--}3$. Downstream of each undulator, an in-vacuum metallic mirror can be inserted to send the FEL radiation to a calibrated photodiode. At the exit of the last undulator, the radiation spectrum is measured using an imaging spectrometer equipped with a diffraction grating and a cooled intensified camera (iCCD). More details are reported in Methods.

The experiment was performed by using driver and witness bunches separated by $\Delta t = 1.21 \pm 0.02$ ps. These are focused at the plasma entrance with the PMQs down to $\sigma_{r,d} = 20 \pm 1 \mu\text{m}$ and $\sigma_{r,w} = 14 \pm 1 \mu\text{m}$, respectively. The driver charge is $Q_d = 200 \pm 5 \text{ pC}$ with duration $\sigma_{t,d} = 215 \pm 5 \text{ fs}$. For the witness, the charge is $Q_w = 20 \pm 2 \text{ pC}$ and the duration is $\sigma_{t,w} = 30 \pm 3 \text{ fs}$. With the plasma turned off, the driver energy is $E_d = 88.5 \pm 0.1 \text{ MeV}$ with energy spread $\sigma_{E,d} = 0.23 \pm 0.01 \text{ MeV}$, whereas for the witness, $E_w = 88.1 \pm 0.1 \text{ MeV}$ and $\sigma_{E,w} = 0.31 \pm 0.02 \text{ MeV}$. The respective initial normalized emittances are $\epsilon_{d,x(y)} = 2.5 \pm 0.2 (1.7 \pm 0.2) \mu\text{m}$ and $\epsilon_{w,x(y)} = 1.4 \pm 0.5 (1.2 \pm 0.4) \mu\text{m}$. All the quantities are quoted as rms. The witness energy chirp is made positive (higher-energy particles on the head) to compensate for the plasma wakefield slope and assist the beam-loading process⁸. Figure 2a shows a single-shot energy spectrum of the driver and witness obtained without plasma on the Ce:YAG screen downstream of the spectrometer.

By turning on the plasma and setting its density to $n_e \approx 1.6 \times 10^{15} \text{ cm}^{-3}$, we obtain the spectrum shown in Fig. 2b. The plot shows both the

accelerated witness and the decelerated driver. Considering 500 consecutive shots of the accelerated witness, its energy and energy spread distributions are reported in Fig. 2c. The resulting average energy is $E_w = 93.9 \pm 0.3 \text{ MeV}$, corresponding to $\approx 200 \text{ MV m}^{-1}$ accelerating gradient. The achieved 0.3 MeV energy jitter is mainly owing to fluctuations of the driver–witness distance and plasma density²⁸. The energy spread of the accelerated witness is preserved, $\sigma_{E,w} = 0.31 \pm 0.08 \text{ MeV}$, whereas its normalized emittance grew to $\epsilon_{w,x(y)} = 2.7 \pm 0.7 (1.3 \pm 0.2) \mu\text{m}$, indicating a transverse mismatch of the beam in the plasma²⁹. Further details are provided in Methods.

Numerical simulations for the plasma wakefield acceleration have been performed with the Architect code³⁰ to support the experimental observations. The interaction between the bunches and the plasma is in the quasi-nonlinear regime³¹, in which the driver density exceeds the plasma density and induces blowout, but – owing to its relatively small charge – the produced perturbation is linear. The driver and witness bunches are thus propagated in a 3-cm-long plasma whose longitudinal profile resembles the experimental one. Figure 2d shows a snapshot of the two bunches propagating in the plasma background. The horizontal and vertical axes represent the co-moving longitudinal (ξ) and radial (r) coordinates. The witness is located in the positively charged region produced by the driver and is accelerated with an average field of $\approx 200 \text{ MV m}^{-1}$, gaining approximately 6 MeV. The bottom plot reports the evolution of the witness energy and energy spread along the capillary longitudinal coordinate z , showing the progressive reduction (that reaches its minimum at $z \approx L_p/2$) and then growth of the energy spread owing to the phase-space rotation during the acceleration process.

Downstream of the capillary, the beam is extracted by means of the second PMQ triplet and matched into the FEL beamline. Passing through the undulators, the beam produces FEL radiation with spectrum peaked at a resonance wavelength $\lambda_r = \lambda_u(1 + K_u^2/2)/2\gamma^2 \approx 830 \text{ nm}$, in which γ is the relativistic Lorentz factor and $K_u \approx 1.4$. A proof of the light amplification along the undulators is provided by measuring the growth of the pulse energy after each undulator with the photodiodes. They collect the light emitted by the witness and driver, as both bunches are transported through the undulators. The latter, however, has a much larger energy spread and is optically mismatched to the FEL beamline lattice. This is sufficient to prevent light amplification from the driver alone, as it was verified by comparing the photodiode signals with and without the witness bunch (see Methods). Figure 3 shows the resulting energies (E_{pd}) measured by the six photodiodes as a function of the longitudinal coordinate (z) at which the light is extracted from the undulators beamline. For each photodiode, 200 consecutive shots were acquired. The values reported correspond to the average energy measured considering only the 10% most intense pulses. An average background signal resulting from the energy-depleted driver was separately measured by turning off the witness

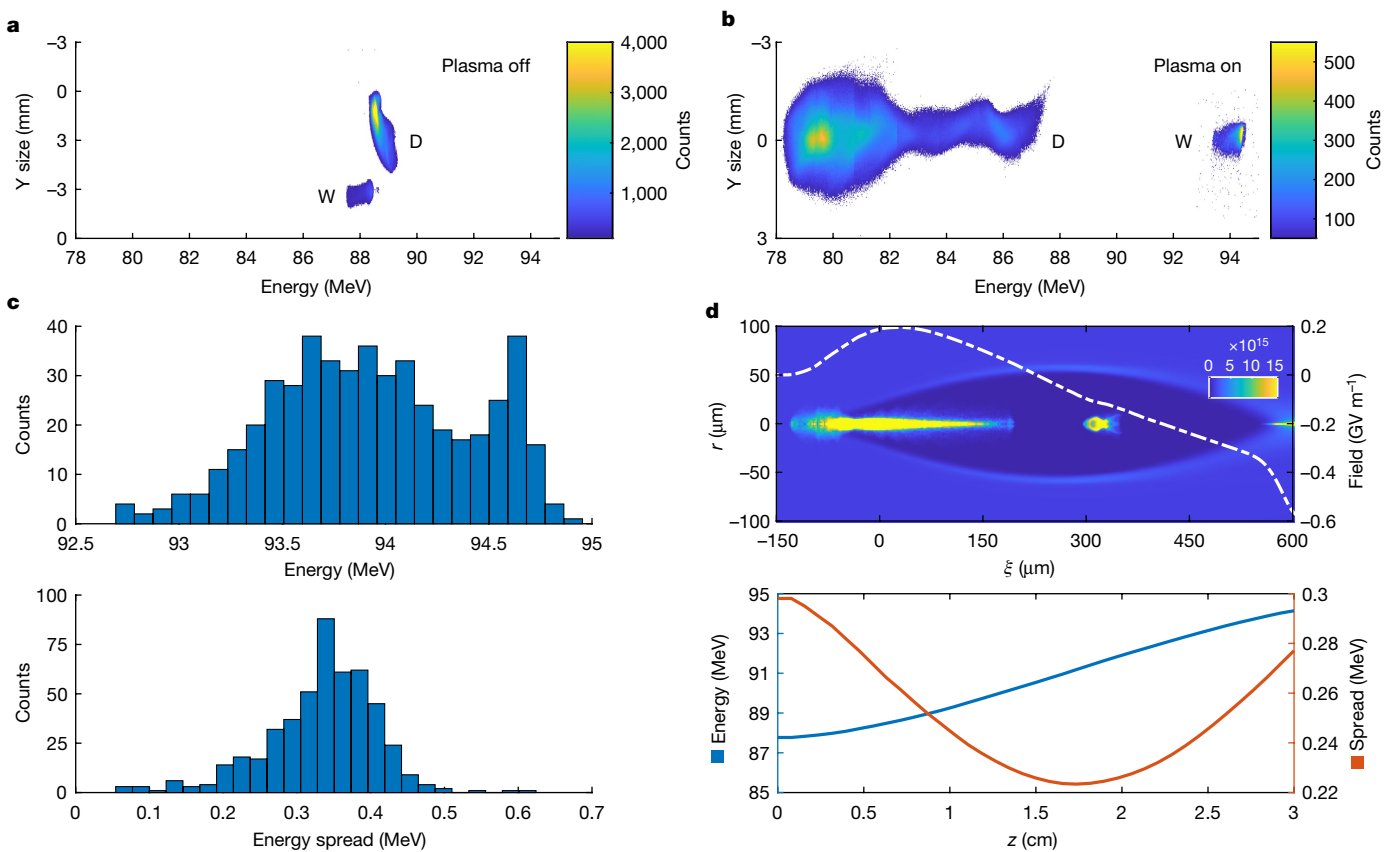


Fig. 2 | Witness acceleration in plasma. Snapshots of the driver (D) and witness (W) spectrum with plasma turned off (**a**) and on (**b**). In **a**, the RF deflector is turned on to vertically separate the two bunches. In **b**, the decelerated driver energy spectrum is obtained by merging the images obtained with different currents of the spectrometer. **c**, Energy (top) and spread (bottom) distributions of 500 consecutive shots of the accelerated

witness. **d**, Numerical simulations. The top plot shows a snapshot of the two bunches moving through the plasma background. The white dashed line shows the axial accelerating field along the co-moving coordinate ξ . The plasma density is reported by the colour bar, in units of cm^{-3} . The evolution of the average energy (blue) and energy spread (red) along the capillary longitudinal coordinate z is reported in the bottom plot.

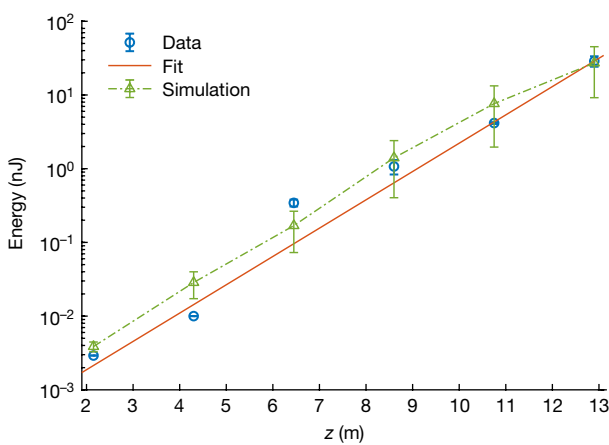


Fig. 3 | Exponential growth of the amplified light. Energy gain of the FEL radiation along the six undulators measured with the photodiodes (blue circles). The red line shows the computed exponential fit over the experimental data. The resulting FEL simulation (green triangles) is also reported. The error bars are computed as the standard deviation of the signal amplitudes measured at each point.

and then subtracted. The red line shows the numerical fit ($R^2 \approx 0.9997$) computed on the measured energy according to the exponential law $E_{\text{pd}} = a \cdot \exp(z/L_g)$, in which $L_g = 1.1 \pm 0.1 \text{ m}$ is the resulting gain length.

Figure 3 also shows a simulation of the amplification process, carried out with the GENESIS 1.3 code³². A set of 100 independent runs was processed similarly to the measured data. The electron beam macroscopic parameters (charge, emittance, energy spread and duration) were statistically varied (within the experimental errors) and used as input for the simulations to estimate the energy fluctuations. The simulated energies reasonably match the measured ones, resulting in a gain length of $L_g = 1.26 \pm 0.13 \text{ m}$, computed on the largest 10% of energies. Considering the SASE regime, large shot-to-shot fluctuations are expected and effectively observed from both the experiment and the simulations³³.

The single-mode amplification of light is supported by the spectral measurements carried out with the imaging spectrometer collecting the light at the end of the undulators beamline. The spectral distributions of the 20 shots with the largest intensities (out of a distribution of 200 samples) is shown in Fig. 4a. The statistical analysis, presented in Fig. 4b, shows that the radiation is centred at $\lambda_r = 826 \pm 9 \text{ nm}$ with bandwidth $\sigma_\lambda = 4.7 \pm 1.1 \text{ nm}$ (corresponding to $\approx 0.6\%$). A single shot of the FEL radiation measured with the imaging spectrometer is shown in Fig. 4c. Good agreement between the simulations and the experiment is confirmed by looking at the simulated spectrum in Fig. 4d. Both plots also report the respective spectrum traces obtained by projecting the images over the horizontal axis.

In conclusion, we reported a proof-of-principle experiment demonstrating the first lasing of a FEL driven by a PWFA. The results indicate that the high quality of the plasma-accelerated beam (with low energy spread and emittance), accompanied by the high stability and reproducibility

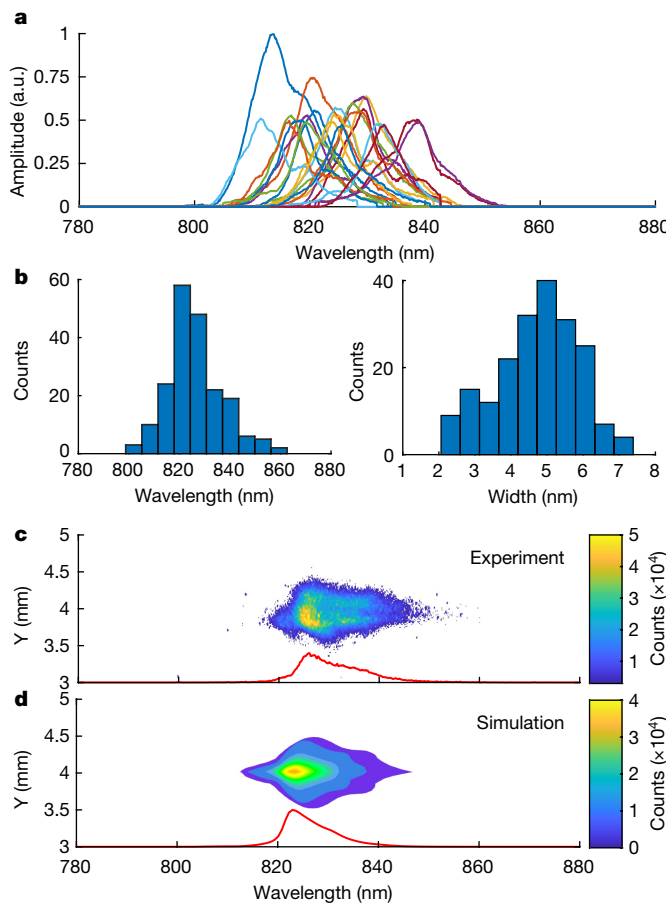


Fig. 4 | Spectral analysis of the amplified light. **a**, Spectral distributions of 20 shots out of 200 selected for the highest pulse energy. **b**, Histograms of 200 consecutive experimental spectra reporting the central wavelength (left) and width (right) of the radiation. **c, d**, 2D traces of single-shot spectra retrieved from experiment (**c**) and simulation (**d**). The horizontal axis maps the wavelength dispersed direction and the vertical axis corresponds to the vertical position on the spectrometer CCD. The red traces in both panels show the spectrum projection on the horizontal axis.

of the acceleration process, allowed to transport the beam along a segmented undulators beamline and amplify FEL light in the near-infrared range. The achieved FEL performances closely match the theoretical expectations thanks to the precise knowledge of the beam phase space, completely characterized from injection and propagation in the plasma up to the capture at its exit. In Methods, we show that such knowledge is fundamental to enable the scalability of this methodology to larger energies and thus to shorter radiation wavelengths. This is also an important contribution in view of EuPRAXIA, a future PWFA-based user facility able to drive an X-rays FEL⁹. In light of similar results achieved with a plasma driven by a laser source¹⁹, with convenience in terms of compactness, realization costs and multistage implementation, here we presented an alternative way to generate FEL amplification from a PWFA, in which the availability of ultra-relativistic particle beams is helpful in terms of acceleration length, repetition rate and overall energetic efficiency. Both techniques demonstrated the generation of electron beams with sufficient quality to induce light amplification in a single-pass FEL. Considering the continuous efforts of the research community to develop ultra-compact accelerators, these results represent an important milestone for next-generation and compact multidisciplinary user facilities.

Online content

Any methods, additional references, Nature Research reporting summaries, source data, extended data, supplementary information, acknowledgements, peer review information; details of author contributions and competing interests; and statements of data and code availability are available at <https://doi.org/10.1038/s41586-022-04589-1>.

- Mangles, S. P. D. et al. Monoenergetic beams of relativistic electrons from intense laser-plasma interactions. *Nature* **431**, 535–538 (2004).
- Faure, J. et al. Controlled injection and acceleration of electrons in plasma wakefields by colliding laser pulses. *Nature* **444**, 737–739 (2006).
- Litos, M. et al. High-efficiency acceleration of an electron beam in a plasma wakefield accelerator. *Nature* **515**, 92–95 (2014).
- Gonsalves, A. J. et al. Petawatt laser guiding and electron beam acceleration to 8 GeV in a laser-heated capillary discharge waveguide. *Phys. Rev. Lett.* **122**, 084801 (2019).
- Nakajima, K. Towards a table-top free-electron laser. *Nat. Phys.* **4**, 92–93 (2008).
- Hartmann, N. et al. Attosecond time-energy structure of X-ray free-electron laser pulses. *Nat. Photonics* **12**, 215–220 (2018).
- Pandey, S. et al. Time-resolved serial femtosecond crystallography at the European XFEL. *Nat. Methods* **17**, 73–78 (2020).
- Pompili, R. et al. Energy spread minimization in a beam-driven plasma wakefield accelerator. *Nat. Phys.* **17**, 499–503 (2021).
- Assmann, R. W. et al. Eupraxia conceptual design report. *Eur. Phys. J. Spec. Top.* **229**, 3675–4284 (2020).
- Argyropoulos, T. et al. Design, fabrication, and high-gradient testing of an X-band, traveling-wave accelerating structure milled from copper halves. *Phys. Rev. Accel. Beams* **21**, 061001 (2018).
- Tajima, T. & Dawson, J. M. Laser electron accelerator. *Phys. Rev. Lett.* **43**, 267 (1979).
- Modena, A. et al. Electron acceleration from the breaking of relativistic plasma waves. *Nature* **377**, 606–608 (1995).
- Sprangle, P., Esarey, E. & Krall, J. Laser driven electron acceleration in vacuum, gases, and plasmas. *Phys. Plasmas* **3**, 2183–2190 (1996).
- Blumenfeld, I. et al. Energy doubling of 42 GeV electrons in a metre-scale plasma wakefield accelerator. *Nature* **445**, 741–744 (2007).
- André, T. et al. Control of laser plasma accelerated electrons for light sources. *Nat. Commun.* **9**, 1334 (2018).
- Deng, A. et al. Generation and acceleration of electron bunches from a plasma photocathode. *Nat. Phys.* **15**, 1156–1160 (2019).
- Lindstrøm, C. A. et al. Energy-spread preservation and high efficiency in a plasma-wakefield accelerator. *Phys. Rev. Lett.* **126**, 014801 (2021).
- Kirchen, M. et al. Optimal beam loading in a laser-plasma accelerator. *Phys. Rev. Lett.* **126**, 174801 (2021).
- Wang, W. et al. Free-electron lasing at 27 nanometres based on a laser wakefield accelerator. *Nature* **595**, 516–520 (2021).
- Chen, P. et al. Acceleration of electrons by the interaction of a bunched electron beam with a plasma. *Phys. Rev. Lett.* **54**, 693 (1985).
- Ferrario, M. et al. SPARC_LAB present and future. *Nucl. Instrum. Methods B* **309**, 183–188 (2013).
- Ferrario, M. et al. Laser comb with velocity bunching: preliminary results at SPARC. *Nucl. Instrum. Methods A* **637**, S43–S46 (2011).
- Serafini, L. & Ferrario, M. Velocity bunching in photo-injectors. *AIP Conf. Proc.* **581**, 87–106 (2001).
- Pompili, R. et al. Femtosecond timing-jitter between photo-cathode laser and ultra-short electron bunches by means of hybrid compression. *New J. Phys.* **18**, 083033 (2016).
- Cianchi, A. et al. Six-dimensional measurements of trains of high brightness electron bunches. *Phys. Rev. Accel. Beams* **18**, 082804 (2015).
- Biagioni, A. et al. Gas-filled capillary-discharge stabilization for plasma-based accelerators by means of a laser pulse. *Plasma Phys. Control. Fusion* **63**, 115013 (2021).
- Pompili, R. et al. Compact and tunable focusing device for plasma wakefield acceleration. *Rev. Sci. Instrum.* **89**, 033302 (2018).
- Romeo, S. et al. Beam-based characterization of plasma density in a capillary-discharge waveguide. *AIP Adv.* **11**, 065217 (2021).
- Shpakov, V. et al. First emittance measurement of the beam-driven plasma wakefield accelerated electron beam. *Phys. Rev. Accel. Beams* **24**, 051301 (2021).
- Marocchino, A. et al. Efficient modeling of plasma wakefield acceleration in quasi-non-linear-regimes with the hybrid code Architect. *Nucl. Instrum. Methods Phys. Res. A* **829**, 386–391 (2016).
- Rosenzweig, J. B. et al. Plasma wakefields in the quasi-nonlinear regime. *AIP Conf. Proc.* **1299**, 500–504 (2010).
- Reiche, S. GENESIS 1.3: a fully 3D time-dependent FEL simulation code. *Nucl. Instrum. Methods Phys. Res. A* **429**, 243–248 (1999).
- Gorobtsov, O. Y. et al. Statistical properties of a free-electron laser revealed by Hanbury Brown-Twiss interferometry. *Phys. Rev. A* **95**, 023843 (2017).

Publisher's note Springer Nature remains neutral with regard to jurisdictional claims in published maps and institutional affiliations.

© The Author(s), under exclusive licence to Springer Nature Limited 2022

Methods

Generation of the two electron bunches

The driver and witness bunches are directly generated on the photocathode by two ultraviolet laser pulses delayed by 5 ps (refs. ^{22,34}). Their relative separation and durations are tuned with the velocity-bunching technique that requires injection in the first travelling-wave section at the zero crossing of the RF wave. The longitudinal compression is then achieved by slightly accelerating the tail of the beam while decelerating its head. This leads to a rotation of the beam longitudinal phase space that is simultaneously chirped and compressed. To avoid uncontrolled emittance growth, solenoids embedded on the linear accelerator are turned on and provide the necessary extra focusing³⁵. Unlike other methods, the velocity bunching does not use any mask or scraper in a dispersive section and therefore there is no loss of charge. The energy chirps of the resulting driver and witness bunches are made complementary by over-compressing the witness (the head and tail are swapped) while under-compressing the driver.

6D phase-space characterization

Longitudinal phase spaces of driver and witness are measured with a RF deflector with a spectrometer dipole. A Ce:YAG screen downstream of the spectrometer is used for the single-shot measurement. The limiting resolution of the optical system is about 5 μm, well below the typical beam size. Taking into account the dimension of the beam without power in the RF deflector, the lens magnification and the camera pixel size, the temporal resolution for energies ≈100 MeV is about 18 fs (ref. ²⁵). For the energy measurement, the ultimate resolution is on the order of 5 keV. Considering also that the RF deflector introduces a further energy spread (≈12 keV in our experimental conditions³⁶), this is still negligible with respect to the measured values for the witness bunch previously reported. The emittance measurement is performed by means of the quadrupole-scan technique³⁷. However, as the driver and the witness are transversely overlapped, the dipole spectrometer is used to separate them in energy, allowing to measure the vertical emittance. The horizontal emittance is measured on the straight line using the RF deflector to separate the bunch vertically. In both cases, the resulting transport matrices have been included in the calculations for the emittance estimation²⁹. As quadrupole scan is a multi-shot technique, at least 20 shots are acquired for every quadrupole current.

Plasma source

For the experiment, a 3-cm-long capillary with a 2-mm-diameter hole has been used. The capillary is 3D printed using photopolymeric material and has two inlets for the gas injection. The capillary is installed in a vacuum chamber directly connected with a windowless, three-stage differential pumping system that ensures 10^{-8} mbar pressure in the RF linac while flowing the gas. This solution allows to transport the beam without encountering any window, thus not degrading its emittance by multiple scattering³⁸. The plasma is produced by ionizing the hydrogen gas produced by water electrolysis (Linde NM Plus Hydrogen Generator). A high-speed solenoid valve, located 5 cm from the capillary, is used to fill the capillary with the gas. The valve is opened for 3 ms and the discharge current is applied 1 ms after its closure. The discharge current, applied to the two capillary electrodes, is generated by a high-voltage generator that provides 5-kV pulses and a current of 120 A through the capillary. The current is monitored with a Pearson current monitor. The plasma density is measured with a Stark-broadening-based diagnostics measuring the $H_{\alpha,\beta}$ Balmer lines³⁹. The stabilization of the discharge process and plasma formation is provided by pre-ionizing the gas with a Quantel 532-nm CFR Ultra Nd:YAG laser, reducing the discharge timing jitter to the order of a few nanoseconds²⁶. The laser is installed close to the capillary vacuum chamber and is injected into it by means of three metallic mirrors, with the last one installed in vacuum close to the capillary entrance. The laser spot diameter at the capillary

entrance is ≈2 mm with energy ≈100 μJ. The best results in terms of the discharge timing jitter (≈1–2 ns) is obtained by pre-ionizing the hydrogen gas confined in the capillary approximately 100 ns before the start of the discharge.

Beam focusing and matching in the plasma

Optimal acceleration without detrimental effects on the emittance requires the witness beam to be transversely matched to the plasma. The matching condition requires a Twiss β-function $\beta_{eq} = \sqrt{\gamma/2\pi r_e n_e}$ to reach an equilibrium solution⁴⁰, with r_e the classical electron radius. For the current experiment, $\beta_{eq} \approx 2.6$ mm, corresponding to a spot size $\sigma_{eq} = \sqrt{\beta_{eq} e_n / \gamma} \approx 5 \mu\text{m}$. The beam focusing at the plasma entrance is obtained by using three PMQs with gradient 520 T m⁻¹ and lengths $L_1 = L_3 = 10.7$ mm and $L_2 = 20.1$ mm. The resulting focal length is $f \approx 13$ cm. The overall focusing of the triplet can be adjusted to match the beam energy by longitudinally moving each PMQ with a nanometre-resolution piezoelectric motor²⁷. A similar triplet of PMQs is installed downstream of the capillary to allow the capture of the high-divergence accelerated witness. The performances of the focusing system with the beam parameters described in this paper allowed to squeeze the witness to a minimum spot size of $\sigma_r \approx 14 \mu\text{m}$, approximately three times larger than the ideal one. This inevitably leads to a deterioration of the emittance during acceleration in the plasma, as experimentally observed here and in previous measurements²⁹. An upgrade of the focusing system is under study at present, with the purpose of shortening the focal length to $f \approx 3$ cm and thus matching the equilibrium solution.

Beam matching in the undulators

The capture and transport of the high-divergence witness coming from the plasma is extremely challenging and require non-trivial manipulations to avoid chromatic aberrations and, in turn, emittance deterioration⁴¹. This task is achieved by using a dedicated triplet of PMQs downstream of the plasma module that gradually catches the beam and matches it into the focusing-defocusing lattice consisting of six conventional electromagnetic quadrupoles located upstream of the FEL beamline. The witness high divergence is removed by the second triplet of PMQs, located approximately 13 cm downstream of the plasma module, that catches the beam and transports it into the FEL. This is shown in Extended Data Fig. 1, in which the Twiss β-function at the exit of the plasma (a few millimetres) is adjusted and matched to the one required by the FEL beamline (a few metres). The transport along the undulators is obtained with a 6.5-m-long transfer line consisting of two triplets of electromagnetic quadrupoles with variable strength. This allows to fit the beam Twiss parameters with the ones required at the undulator entrance to optimize the FEL performance. The undulator line consists of six modules each one 2.15 m long. Owing to the low energy of the beam, the focusing effects of the undulators⁴² is not negligible, with each undulator acting as a transport element in the magnetic lattice once the resonance wavelength and undulator gaps are set. The optimum beam matching is ensured by means of short electromagnetic quadrupoles located between the undulators that allow to horizontally focus the beam at the undulator entrance. The vertical focusing, instead, is provided by the undulators themselves. This allows to use both the undulators and the quadrupoles as an overall focusing-defocusing cell. The exact values of the quadrupoles strengths are found by means of a dedicated algorithm that minimizes the average transverse beam size along the undulators. Extended Data Figure 1 shows the resulting evolution of the β and α Twiss functions downstream of the plasma stage, passing through the second PMQ triplet and the FEL beamline.

FEL radiation detection and analysis

The energy gain of the FEL radiation is measured by means of six silicon photodiodes installed downstream of each undulator. The radiation is extracted by inserting an in-vacuum high-reflective mirror.

Article

The photodiodes (Thorlabs PDA100A), whose response was previously calibrated using a reference 800-nm laser, collect the light through a focusing lens and their signals are read with a digital scope (LeCroy WS454). Neutral density filters have been used to avoid signal saturation, especially for the photodiode downstream of the last undulator. Here the FEL radiation is also transported to the imaging spectrometer (HORIBA iHR320). An imaging system consisting of several mirrors and a lens with a focal length of 30 cm make a 3:1 magnification of the FEL radiation transverse size at the spectrometer entrance slit. The spectrometer has a diffraction grating with 600 lines per mm and can be rotated to accommodate wavelengths in the 400–900-nm spectral range. The dispersed light is then measured with a cooled intensified camera (Andor iStar 720) with a spectral resolution of 0.12 nm per pixel. The entire spectral window available with such a configuration is about 120 nm.

Extended Data Figure 2 shows the measured energies of the FEL radiation detected with the photodiode downstream of the last undulator. The plot reports: (1) the total energies coming from both the driver and the witness bunches, (2) the background induced by the unamplified driver only and (3) the resulting energies owing to the witness after subtracting the average driver background. Although an important contribution to the observed intensity fluctuations comes from the jittering of the plasma-accelerated witness (in terms of energy, spread and emittance), here we also compare the data with theoretical expectations. This is done by assuming that the radiation energy (E) follows the distribution $\Gamma \sim (E/\bar{E})^{M-1} \cdot \exp(-M \cdot E/\bar{E})$ with relative standard deviation $1/\sqrt{M}$, in which $M \approx \sigma_{z,w}/l_c$ with $\sigma_{z,w}$ the witness bunch length and l_c the cooperation length⁴³. As the expected cooperation length is $\approx 30 \mu\text{m}$ (that is, $\approx 100 \text{ fs}$), it results in $M \approx 0.3$. The plot shows an overall good agreement with the theoretical curve, with some expected deviations (not resulting from the SASE shot noise) coming from intrinsic fluctuations of the main beam parameters.

Plasma wakefield simulations

The interaction between the driver and the witness electron bunches with the plasma background is simulated with Architect³⁰, a hybrid code in which the relativistic electron bunches are treated kinetically as in a particle-in-cell code and the background plasma as a fluid. The code has been widely validated through direct comparisons with full particle-in-cell codes, showing a remarkable agreement⁴⁴. The simulation described here has been obtained with 4×10^5 macro-particles for the two bunches and a longitudinal (transverse) 2-μm (1-μm) mesh resolution. The plasma density profile is computed to reproduce the profile measured experimentally. The advancing time step is set to 1.2 fs to guarantee a correct sampling of both driver and witness.

FEL simulations

FEL emission was simulated with the three-dimensional code GENESIS 1.3 (ref. ³²) used in the time-dependent mode, with the maximum available precision (mesh resolution equal to λ_r , temporal step equal to λ_r/c). The witness electron beam microscopy is randomly changed in a set of 100 independent runs, in which jitters of about 10% for the bunch charge, length and emittance are taken into account. The spectral analysis is carried out by post-processing the simulation data with an algorithm able to model the spectrometer input slit or grating transformations to reproduce the spectrum collected on the camera. The resulting average bandwidth from simulations is $\Delta\lambda_r = 5.88 \pm 0.68 \text{ nm}$, average size of the radiation is $4.08 \pm 0.14 \text{ mm}$ and its divergence is $1.16 \pm 0.07 \text{ mrad}$. The mean value of the energy extracted at the end of the last undulator is $\approx 27 \text{ nJ}$, with fluctuations of about 100% if the entire distribution of 100 simulations is considered. They are mainly owing to the jitters of the macroscopic beam parameters and the microscopic shot noise initiating the amplification process. The resulting average radiation length is $47 \pm 5 \mu\text{m}$ (rms). A typical simulated single-spike power temporal profile is shown in Extended Data Fig. 3.

The exponential decay of the intensity associated to the time the radiation has left the electron bunch is shown on the pulse leading edge, whereas the modulations on the intensity highlight the positions where the beam crosses the undulator gaps.

Scaling of the assisted beam-loading technique

In a plasma wakefield accelerator, the beam-loading process is usually described by superimposing the wakefield generated by the trailing bunch onto that of the driver to yield the final accelerating field. A controlled shaping of the witness longitudinal profile is thus required to remove the plasma wake slope and avoid energy spread growth⁴⁵. In a recent work we also demonstrated that beam loading can be assisted by setting a positive energy chirp (higher-energy particles on the head of the bunch) on the witness to pre-compensate the plasma wake slope⁸. To show how such a technique can be extended, we use the analytical model developed for the quasi-nonlinear regime to evaluate the amount of energy chirp that is required for a specific configuration. By describing the blowout region as an ellipsoid with normalized radial and longitudinal semi-axes $R_b = 2\sqrt{\alpha} k_p \sigma_r$ (with $\alpha = n_b/n_p$ and n_b the bunch density) and $L_b = k_p \lambda_p / 2 = \pi$, the axial electric field can be written as $E_b(z) = -f_b \frac{en_p}{\epsilon_0} \cdot z$, with $f_b = R_b / 3L_b$, e the electron charge, ϵ_0 the vacuum dielectric constant and z the distance from the geometric centre of the ellipsoid. Considering thus the field produced by the driver (E_d) and witness self-field (E_w), the overall electric field acting on the latter is given by

$$E_z(z) = E_d(z) - \frac{1}{2}E_w(z) = -\frac{en_p}{\epsilon_0} \left(f_d - \frac{1}{2}f_w \right) \cdot z, \quad (1)$$

with the factor 1/2 taking into account the fundamental theorem of beam loading⁴⁶. Similarly, the expression of the radial field acting on the witness reads as

$$E_r(r) = -\frac{en_p}{2\epsilon_0} \left(1 - f_d \right) \cdot r. \quad (2)$$

From equation (1), we can compute the energy chirp α_i required to completely compensate the wake slope over an acceleration length L_c as

$$\begin{aligned} \alpha_i &= -eL_c \cdot \frac{d}{dz} \left[E_d(z) - \frac{1}{2}E_w(z) \right] \\ &= \frac{e^2 n_p}{\epsilon_0} \left[f_d - \frac{1}{2}f_w \right] \cdot L_c \end{aligned} \quad (3)$$

Considering the PWFA scenario, the amount of energy chirp imprinted on a bunch is easily handled by adjusting the linac RF phases, for example, at SPARC_LAB, it can be tuned in the range $\alpha_i \approx -10\text{--}90 \text{ GeV m}^{-1}$ (ref. ⁸).

Extended Data Figure 4 (top) shows the simulated wakefield reported in Fig. 2d together with its analytical approximation and highlights a good agreement between the two. The bottom plot reports the energy chirp required as a function of L_c and for several witness charges to achieve the minimum energy spread at the exit of the PWFA. Large energy chirps allow to accomplish the energy spread minimization over longer lengths and the same applies to high bunch charges, enhancing the beam loading. These values have been computed for the plasma and driver parameters reported in the manuscript, thus keeping the accelerating field fixed. The plot shows that final energies $\approx 140 \text{ MeV}$ are achievable, that is, $\approx 55\%$ larger than the initial energy provided by the linac only. The evolution of the energy spread along L_c is shown in Extended Data Fig. 5a. Here we assumed the use of the largest energy chirp achievable at SPARC_LAB ($\alpha_i \approx 90 \text{ GeV m}^{-1}$) to demonstrate the scalability of the assisted beam-loading technique. For the sake of completeness, a comparison with the energy spread

obtained without using such a technique (that is, by setting $\alpha_i = 0$) is also reported. The initial projected energy spread is computed as $\sigma_E = \sqrt{\sigma_{E,u}^2 + \alpha_i^2 \cdot \sigma_{z,w}^2}$, with $\sigma_{E,u} = 0.2$ MeV being the uncorrelated energy spread and the second term representing the correlated energy spread. The plot shows that the energy spread is minimized at specific $L_c = L_c^*$, depending on the witness charge. For $L_c \geq L_c^*$, the beam longitudinal phase space is over-rotated so that the projected energy spread monotonically grows and at $L_c = 2L_c^*$, its value is equal to the initial value. The plot shows that, with a proper choice of the initial chirp and witness charge, the energy spread can be minimized for any L_c^* . Moreover, for $L_c \geq L_c^*$, the assisted beam-loading technique always generates smaller energy spreads (with respect to the cases with $\alpha_i = 0$).

Non-negligible energy spreads can induce also detrimental effects on the normalized emittance. Particles with different energies indeed rotate with different velocities in the transverse phase space, widening the bunch trace-space area. The resulting projected normalized emittance therefore becomes a function of both propagation length and energy spread⁴⁷. These effects are even enhanced if the bunch is not transversely matched to the plasma. As a cross-check of the model with the experiment, Extended Data Fig. 5b shows the evolution of the energy spread and emittance using the experimental parameters for the witness and the plasma. The emittance is computed by propagating the bunch macro-particles in the blowout region, whose focusing field is computed with equation (2). In this case, the growth is owing to both chromatic effects and the transverse mismatch.

However, a careful choice of the initial witness parameters allows to minimize both effects. This is shown in Extended Data Fig. 6a, in which the emittance is computed as a function of L_c for several witness configurations. At the plasma entrance, the beam is assumed to be transversely matched to the plasma ($\sigma_r = \sigma_{eq} \approx 5 \mu\text{m}$) with normalized emittance $\epsilon_n \approx 1 \mu\text{m}$. When the witness energy chirp is optimized for a specific L_c , the (unavoidable) emittance growth resulting from chromatic effects is below 7%. Conversely, a much larger emittance growth is observed for the unchirped witness (up to $\approx 20\%$), with the growing energy spread inducing larger chromatic effects. It is worth pointing out that, in any case, the resulting emittance is ultimately determined by transverse matching at the plasma entrance. If the spot size does not satisfy the matching condition, large envelope oscillations build up, followed by a growth of the emittance. Extended Data Figure 6b is obtained with $\sigma_r = 14 \mu\text{m} \gg \sigma_{eq}$. Also in this case, the use of the initial energy chirp helps to reduce the final emittance that would be reached without it. The plot highlights that the main contribution to the emittance deterioration is now represented by the transverse mismatch of the witness, rather than by chromatic effects.

EuPRAXIA design study

Considering the control of the acceleration process and FEL lasing achieved at SPARC_LAB, we have performed a complete study on the basis of start-to-end simulations to demonstrate the possibility to extend the same methodology to larger beam energies and, thus, shorter FEL wavelengths. The study is performed within the EuPRAXIA collaboration⁹ that foresees the realization of two plasma-based FEL facilities on the basis of the use of PWFA and laser-driven wakefield accelerator. The results of the study are given in the following, showing the feasibility to obtain FEL emission in the X-rays range by using a GeV energy beam accelerated by a PWFA stage⁴⁸. The PWFA pillar of EuPRAXIA will adopt a linac to produce the driver and witness bunches. It consists of a high-brightness photo-injector that exactly resembles the SPARC_LAB one, with very similar beam parameters. Downstream of the injector, a booster will be used to accelerate from ≈ 100 MeV to ≈ 500 MeV (ref. ⁴⁹). The bunches are then injected in a 40-cm plasma module to accelerate the witness up to ≈ 1 GeV. Numerical simulations for the beam–plasma interaction foresee a resulting accelerating field of $E_z \approx 1.2 \text{ GV m}^{-1}$ by operating at $n_e \approx 10^{16} \text{ cm}^{-3}$ density. This is achieved by using a 200-pC driver with a duration of 200 fs, followed

by a 30-pC witness with a duration of 10 fs. Extended Data Figure 7 shows the expected longitudinal phase space at the plasma exit. The simulations provide a high-brightness witness with peak current ≈ 2.6 kA and $\sigma_{E,w} \approx 0.7\%$ with $\epsilon_w \approx 0.4 \mu\text{m}$ normalized emittance. These numbers show that the resulting quality is comparable with state-of-the-art machines, thus enabling the subsequent injection of the witness in a FEL beamline.

Similarly to the SPARC_LAB experimental setup, this task is accomplished by extracting the witness from the PWFA stage by using a triplet of PMQs. The bunch is then transported to a 30-m-long FEL beamline to demonstrate the generation of coherent radiation centred at $\lambda_r \approx 3 \text{ nm}$ (ref. ⁵⁰). Assuming an undulator period of $\lambda_u = 1.5 \text{ cm}$ with $K = 1.13$, the 3D FEL parameter⁵¹ evaluated for the witness slice parameters is $\rho_{3D} \approx 1.9 \times 10^{-3}$, with a resulting gain length $L_g \approx 0.37 \text{ m}$. The growth of the radiation, as given by simulations with GENESIS 1.3, is shown in Extended Data Fig. 8. The saturation length is $\approx 20 \text{ m}$, with an emitted energy of about 6.5 μJ (corresponding to an average power of $\approx 1.6 \times 10^8 \text{ W}$) and $\approx 10^{11}$ photons per shot. The inset shows the radiation spectrum at the end of the beamline. The start-to-end simulation highlights that the integration of a PWFA stage in a FEL user facility is possible, making it competitive (in terms of size and costs) with other realities on the basis of conventional accelerators. Although such an integration requires non-trivial manipulations of the beam to allow its proper transport along the entire machine, the results on the FEL emission provide a solid base for the correct extension of the experimental results provided here in a larger context represented, for instance, by EuPRAXIA.

Data availability

The data that support the findings of this study are available from the corresponding author on reasonable request.

34. Pompili, R. et al. Time-resolved study of nonlinear photoemission in radio-frequency photoinjectors. *Opt. Lett.* **46**, 2844–2847 (2021).
35. Ferrario, M. et al. Experimental demonstration of emittance compensation with velocity bunching. *Phys. Rev. Lett.* **104**, 054801 (2010).
36. Behrens, C. & Gerth, C. On the limitations of longitudinal phase space measurements using a transverse deflecting structure. *Proc. DIPAC09 TUPB44* (2009).
37. Löhl, F. & Schreiber, S. et al. Measurements of the transverse emittance at the FLASH injector at DESY. *Phys. Rev. Accel. Beams* **9**, 092802 (2006).
38. Pompili, R. et al. Focusing of high-brightness electron beams with active-plasma lenses. *Phys. Rev. Lett.* **121**, 174801 (2018).
39. Biagioni, A. et al. Temperature analysis in the shock waves regime for gas-filled plasma capillaries in plasma-based accelerators. *J. Instrum.* **14**, C03002 (2019).
40. Barov, N. & Rosenzweig, J. B. Propagation of short electron pulses in underdense plasmas. *Phys. Rev. E* **49**, 4407 (1994).
41. Rossetti Conti, M. et al. Electron beam transfer line design for plasma driven free electron lasers. *Nucl. Instrum. Methods Phys. Res. A* **909**, 84–89 (2018).
42. Quattromini, M. et al. Focusing properties of linear undulators. *Phys. Rev. Accel. Beams* **15**, 080704 (2012).
43. Hogan, M. et al. Measurements of high gain and intensity fluctuations in a self-amplified, spontaneous-emission free-electron laser. *Phys. Rev. Lett.* **80**, 289 (1998).
44. Massimo, F., Atzeni, S. & Marocchino, A. Comparisons of time explicit hybrid kinetic-fluid code Architect for plasma wakefield acceleration with a full PIC code. *J. Comput. Phys.* **327**, 841–850 (2016).
45. Tzoufras, M. et al. Beam loading in the nonlinear regime of plasma-based acceleration. *Phys. Rev. Lett.* **101**, 145002 (2008).
46. Chao, A. W. et al. *Handbook of Accelerator Physics and Engineering* (World Scientific, 2013).
47. Arinello, R. et al. Transverse beam dynamics in a plasma density ramp. *Phys. Rev. Accel. Beams* **22**, 041304 (2019).
48. Ferrario, M. et al. EuPRAXIA@SPARC_LAB design study towards a compact FEL facility at LNF. *Nucl. Instrum. Methods Phys. Res. A* **909**, 134–138 (2018).
49. Vaccarezza, C. et al. EUPRAXIA@SPARC_Lab: beam dynamics studies for the X-band Linac. *Nucl. Instrum. Methods Phys. Res. A* **909**, 314–317 (2018).
50. Petrillo, V. et al. Free electron laser in the water window with plasma driven electron beams. *Nucl. Instrum. Methods Phys. Res. A* **909**, 303–308 (2018).
51. Huang, Z. & Kim, K. J. Review of x-ray free-electron laser theory. *Phys. Rev. Accel. Beams* **10**, 034801 (2007).

Acknowledgements This work has been partially supported by the European Commission in the Seventh Framework Programme, grant agreement 312453-EuCARD-2, the European Union Horizon 2020 research and innovation programme, grant agreement no. 653782 (EuPRAXIA), the INFN with the GRANT73/PLADIP grant, SL_COMB2FEL and PLASMAR collaboration with the

Article

ENEA FSN-FUSPHY Division. The work of A.Z. was partially supported by the ISF foundation. We thank D. Pellegrini for the development of the high-voltage discharge pulser and F. Anelli, M. Del Franco and A. Liedl for the technical support. We also thank all the machine operators involved in the experimental run.

Author contributions M.F., E.C., A.C., A.P. and R.P. planned the experiment. A.P. and R.P. managed the experiment, with inputs from all the co-authors. A.B. provided the plasma characterization. A.P. and A.S. managed the FEL beamline. G.C. and M.G. managed the FEL diagnostics. A.C. and V.S. managed the beam diagnostics. F.V. managed the photocathode laser system. R.P. carried out the data analysis. A.D.D. provided numerical simulations for the beam-plasma interaction. F.N., M.O. and V.P. provided numerical simulations for the FEL. R.P.

and L.G. wrote the manuscript. All authors were involved in the experiment, extensively discussed the results and reviewed the manuscript.

Competing interests The authors declare no competing interests.

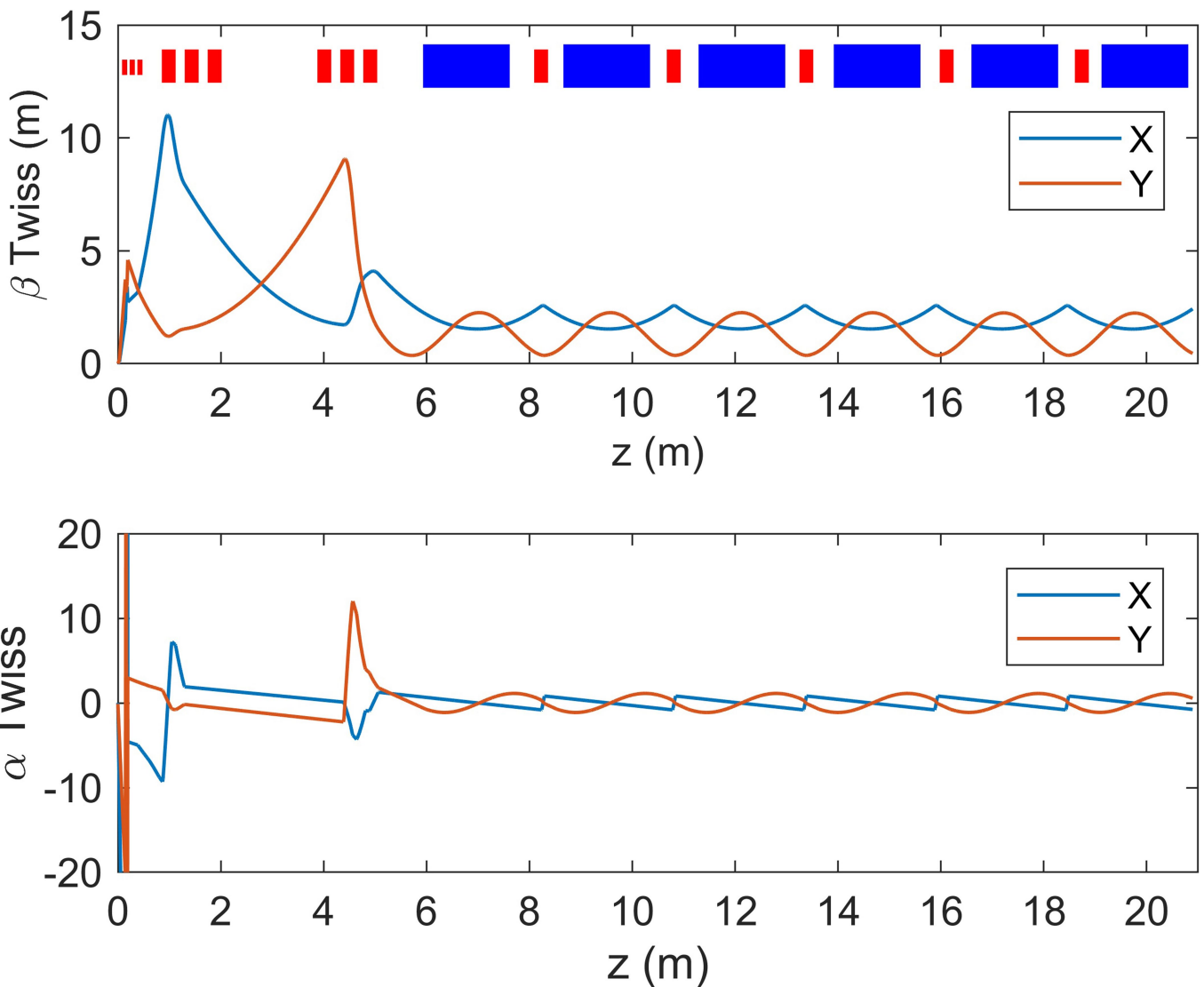
Additional information

Supplementary information The online version contains supplementary material available at <https://doi.org/10.1038/s41586-022-04589-1>.

Correspondence and requests for materials should be addressed to R. Pompili.

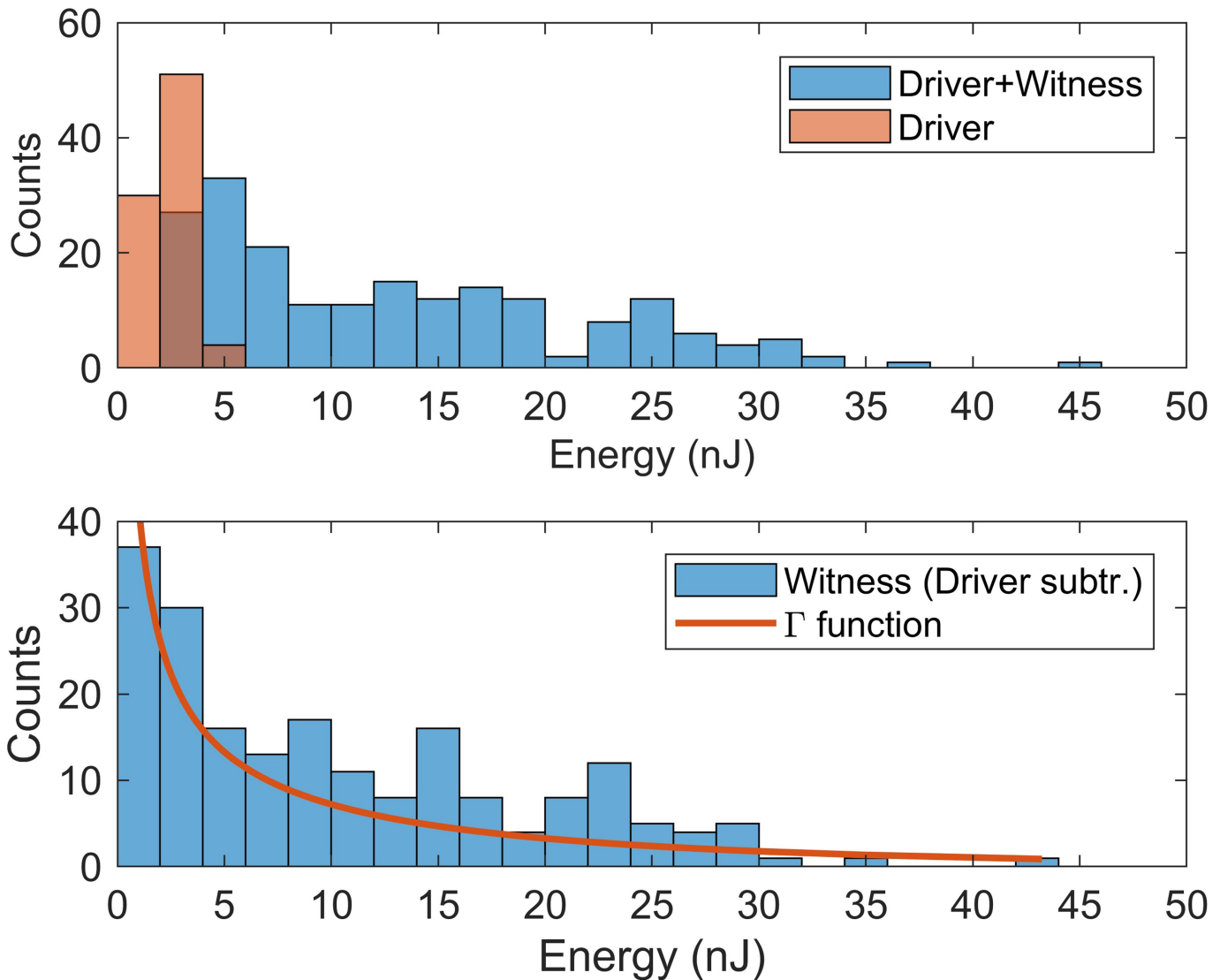
Peer review information *Nature* thanks James Rosenzweig and the other, anonymous, reviewers for their contribution to the peer review of this work. Peer reviewer reports are available.

Reprints and permissions information is available at <http://www.nature.com/reprints>.



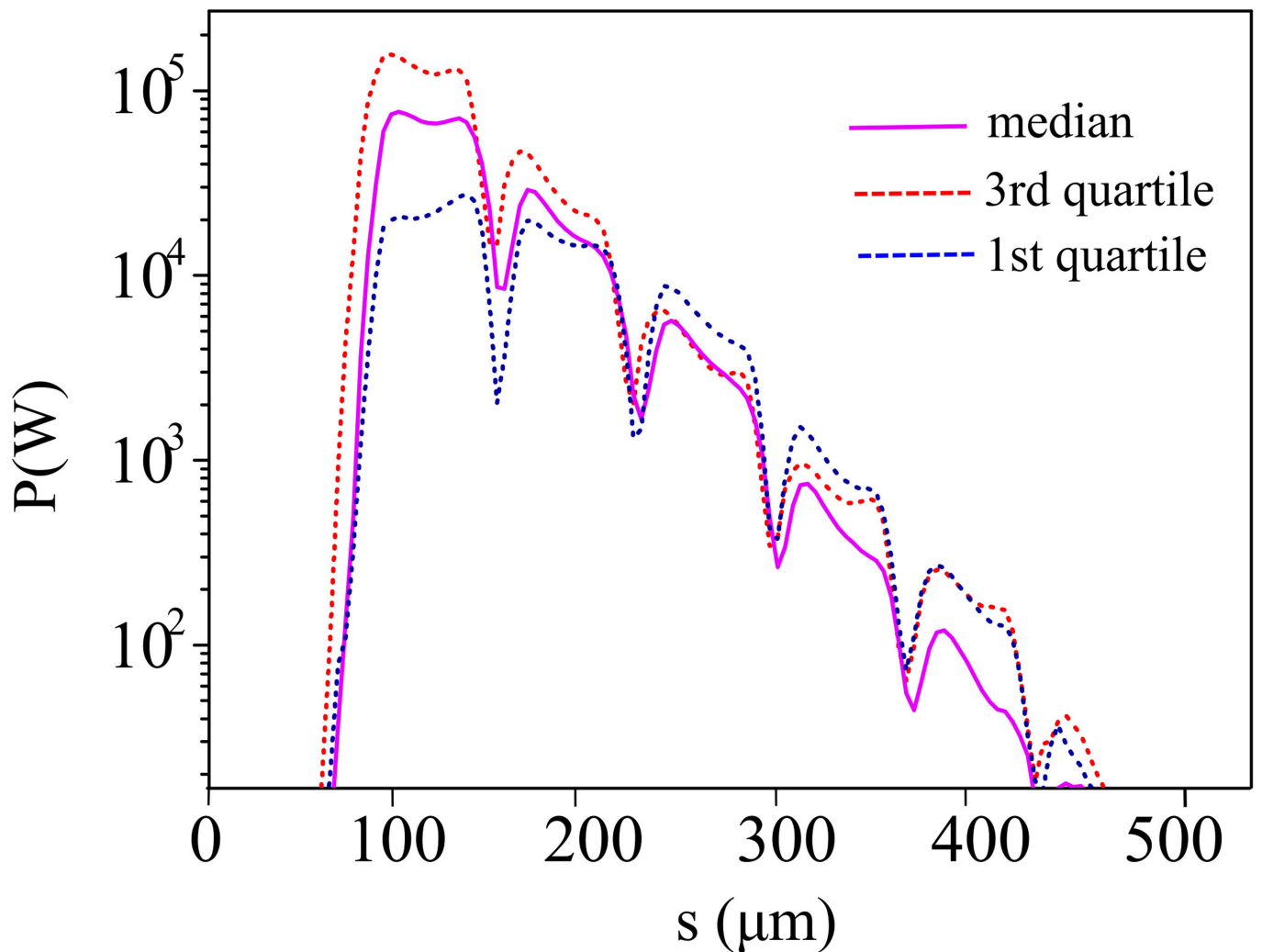
Extended Data Fig. 1 | Evolution of the Twiss parameters. Twiss $\beta_{x,y}$ (top) and $\alpha_{x,y}$ (bottom) functions downstream of the plasma stage, passing through the second PMQ triplet and the FEL beamline as computed by the dedicated

algorithm. The position of the transport quadrupoles and undulators is reported with the red and blue rectangles, respectively.

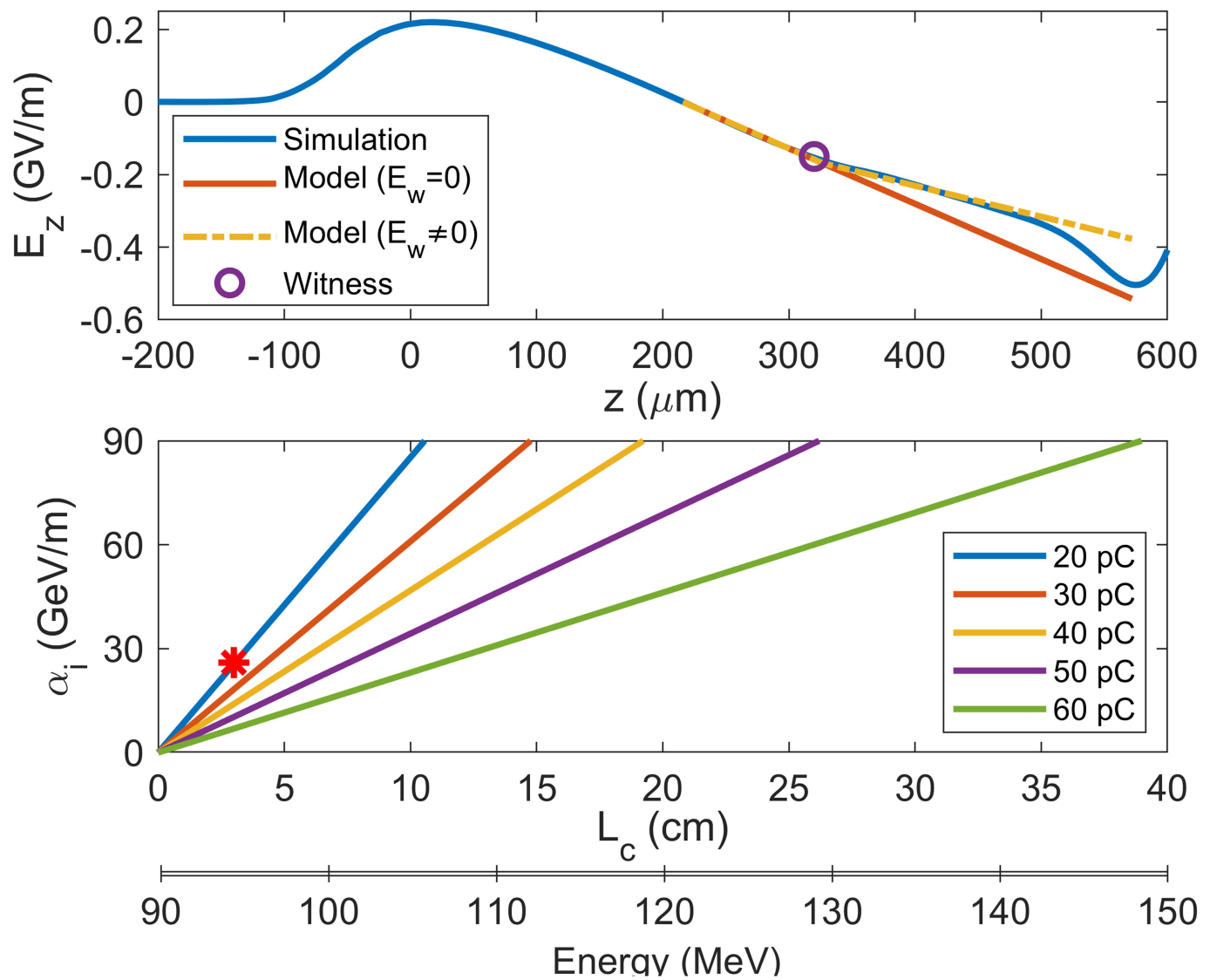


Extended Data Fig. 2 | Energies of the detected FEL radiation. The total signals, collected downstream of the last undulator and coming from both driver and witness bunches, are reported on the top. The witness signals with

subtracted background coming from the driver are reported on the bottom. The intensity fluctuations of the detected radiation are compared with the theoretical Γ function.

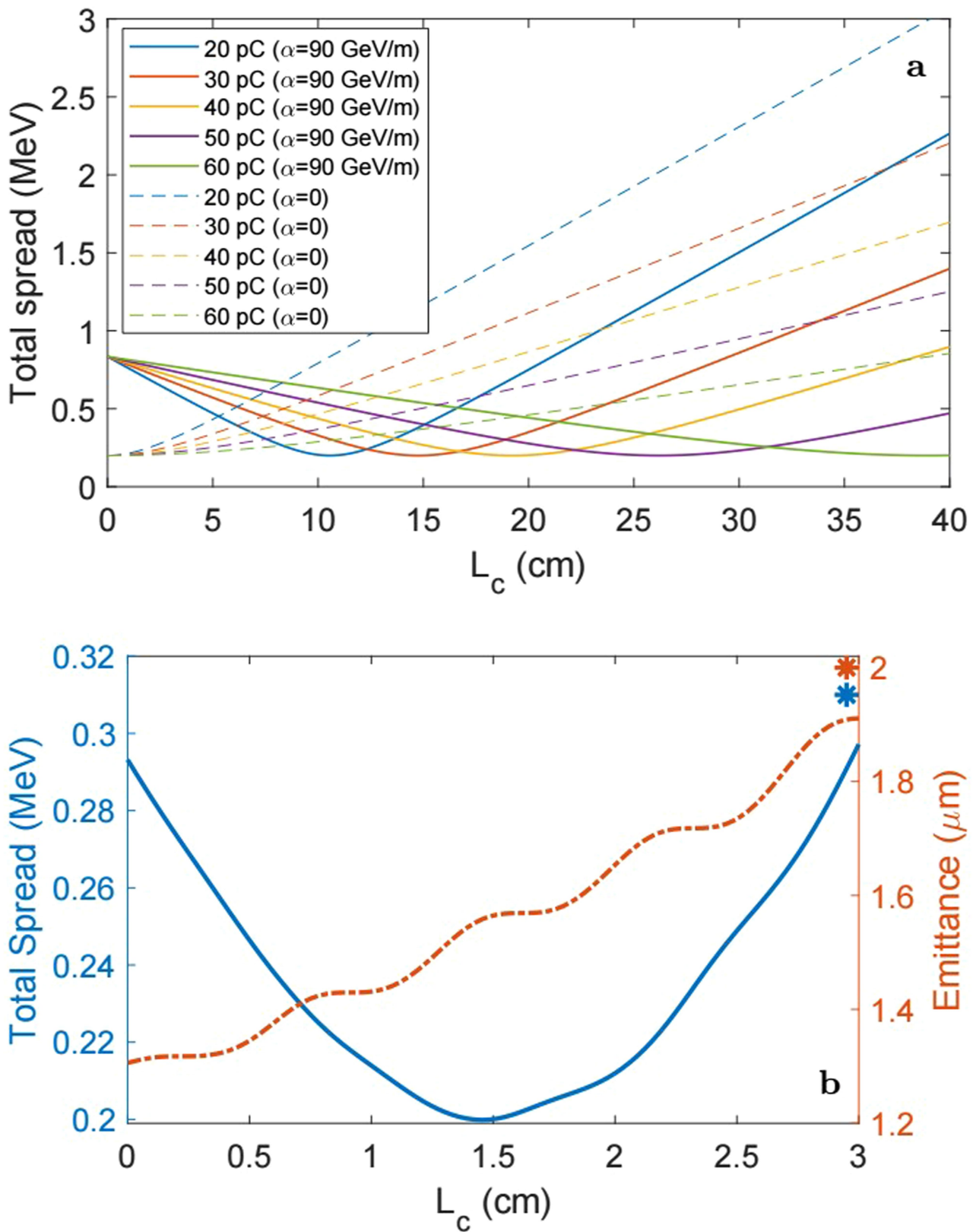


Extended Data Fig. 3 | Power distribution. Simulated output power distribution (P) versus s extracted after the sixth undulator. Statistical median in violet, first and third quartiles are reported in blue and red, respectively.



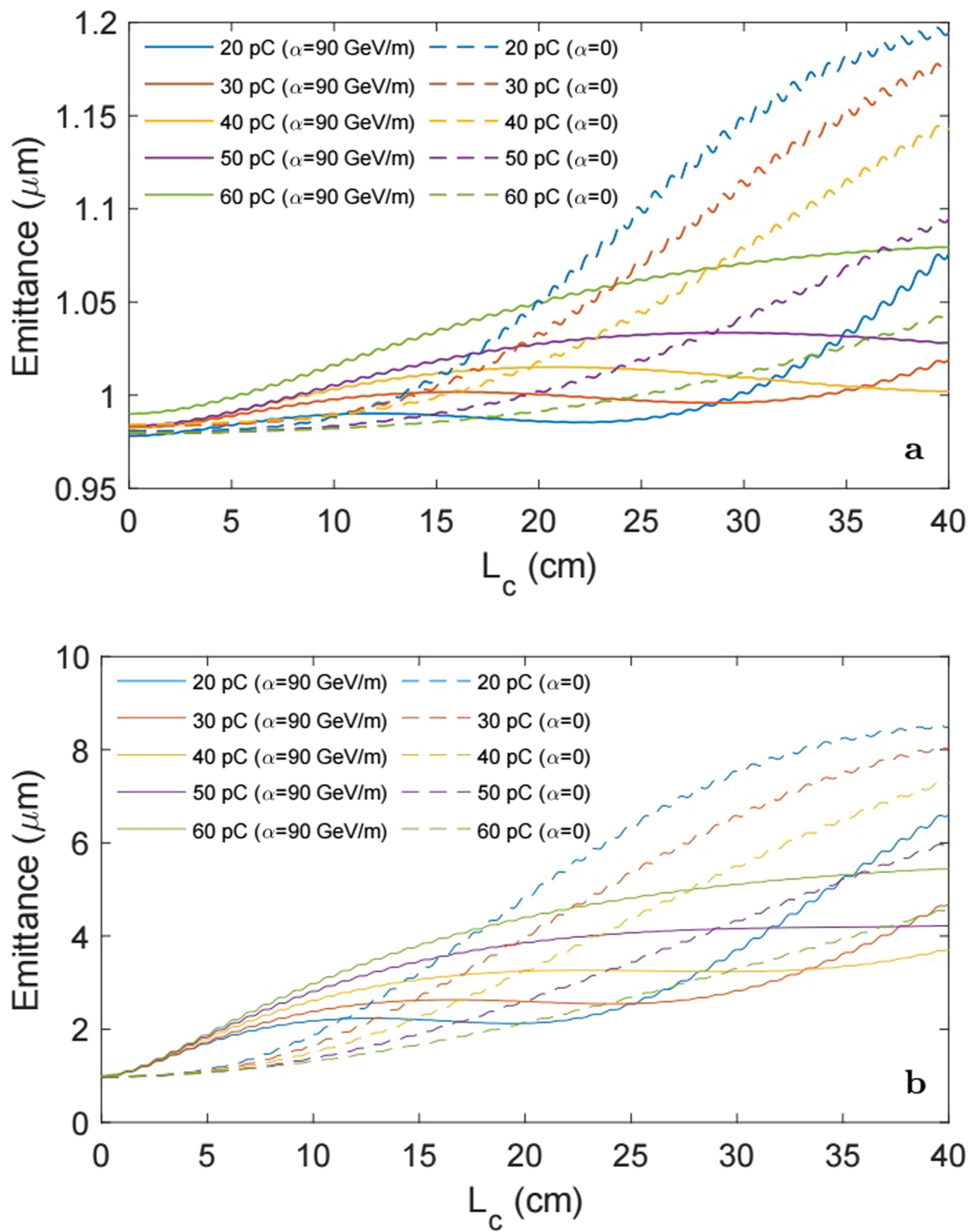
Extended Data Fig. 4 | Energy scaling. Top, analytic approximation of the plasma wakefield reported in Fig. 2d. The red (yellow) line shows the field computed without (with) the witness beam loading. Bottom, scaling of the energy chirp α_i needed to minimize the witness energy spread as a function of

L_c . The calculation is performed for several witness charges. The red asterisk refers to the configuration used in the current experiment. The x-axis also reports the resulting final energy.



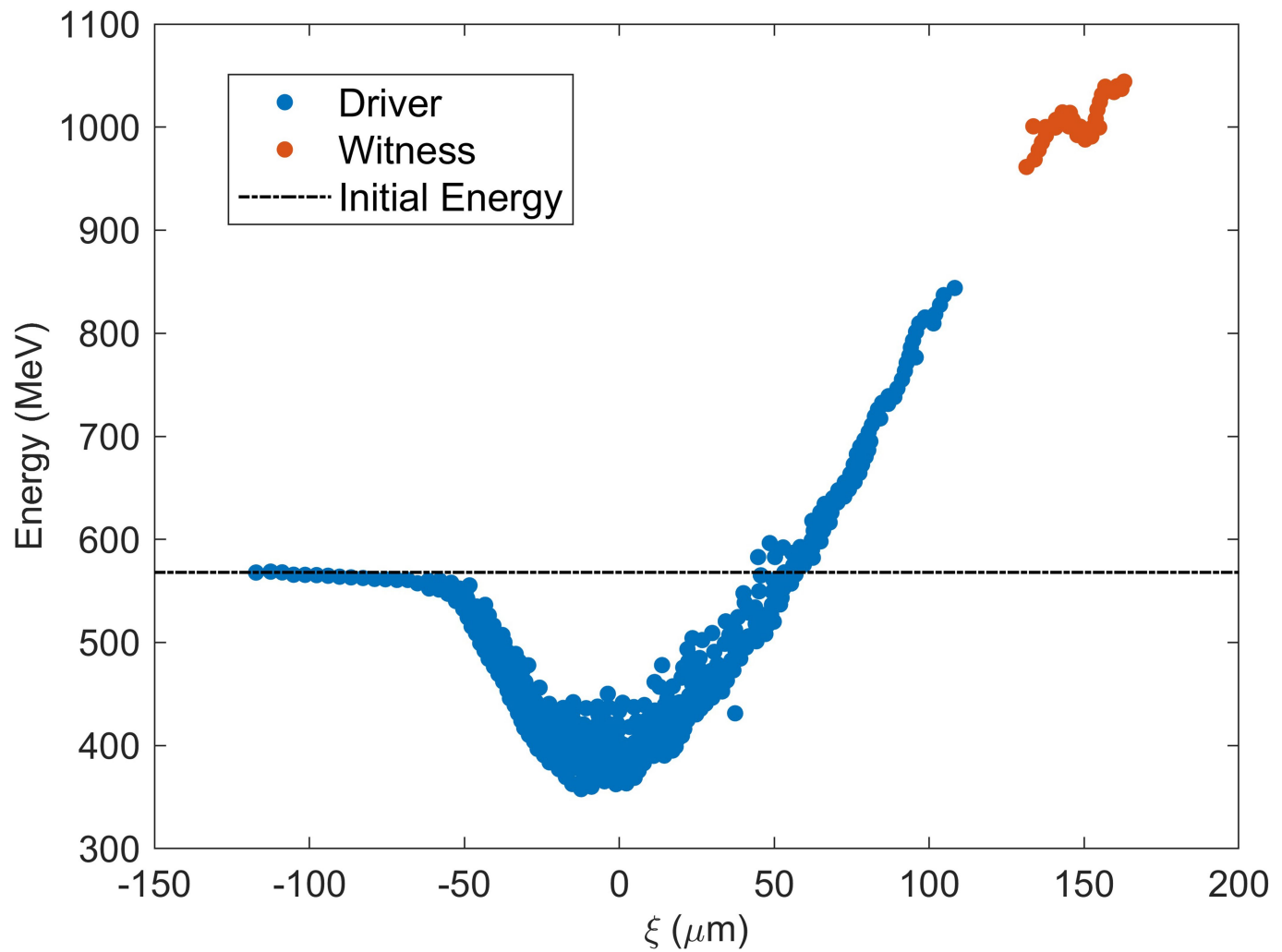
Extended Data Fig. 5 | Energy spread evolution. **a**, Evolution of the energy spread as a function of the plasma acceleration length L_c for several witness charges. The solid (dashed) lines are computed assuming an initial energy

chirp $\alpha_i \approx 90 \text{ GeV m}^{-1}$ ($\alpha_i = 0$). **b**, Energy spread and emittance evolution evaluated for the witness beam parameters used in the experiment. The asterisks refer to the experimentally measured values.

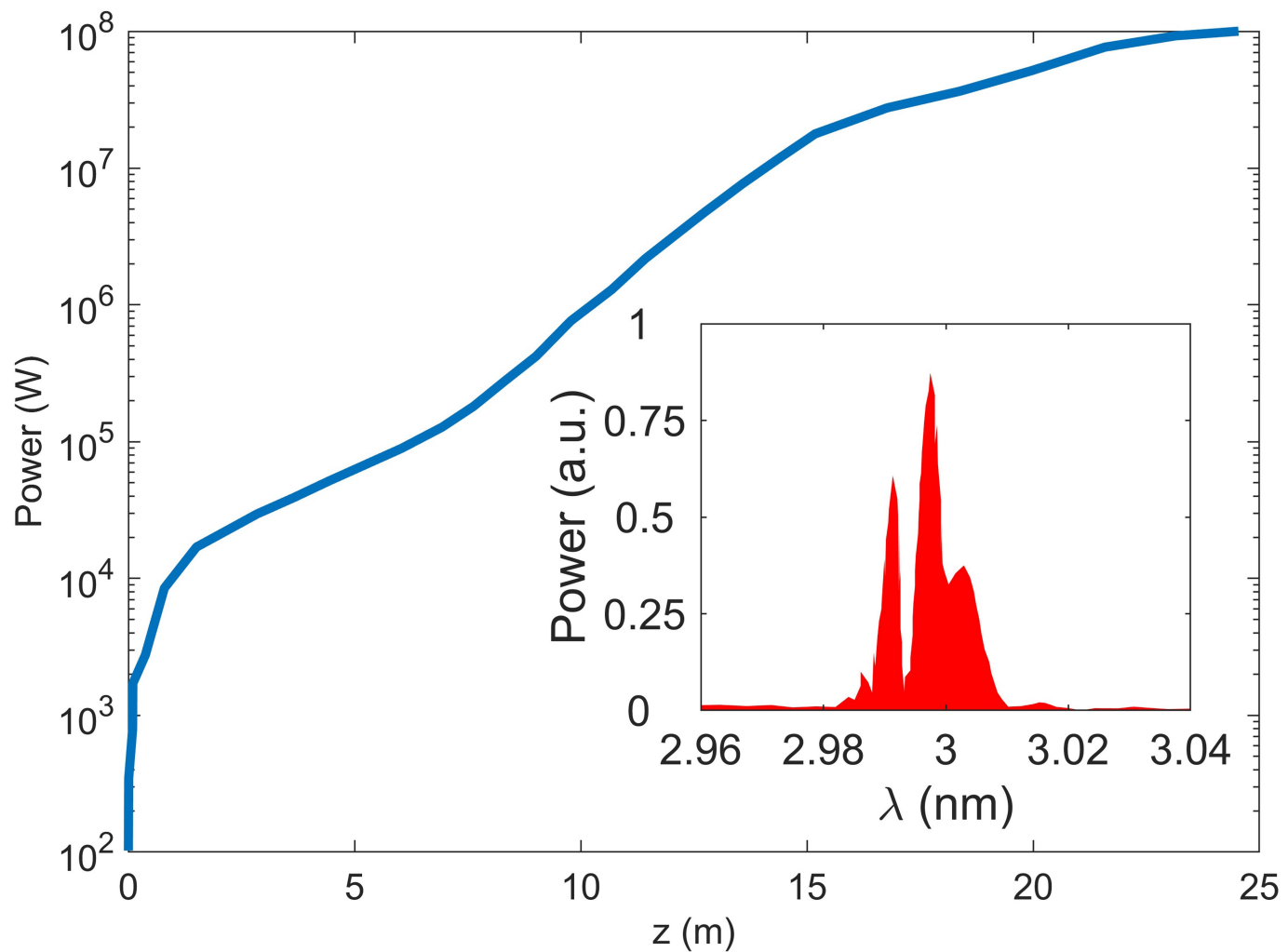


Extended Data Fig. 6 | Emittance evolution. Normalized emittance as a function of the plasma acceleration length L_c with a transversely matched (**a**, $\sigma_r = \sigma_{eq}$) and unmatched (**b**, $\sigma_r = 14 \mu\text{m} \gg \sigma_{eq}$) witness beam for several

charges. The solid (dashed) lines are computed assuming an initial energy chirp $\alpha_i \approx 90 \text{ GeV m}^{-1}$ ($\alpha_i = 0$).



Extended Data Fig. 7 | Plasma-accelerated beams at EuPRAXIA. Longitudinal phase space of both driver and witness. The dashed line shows the beam energy at the plasma entrance.



Extended Data Fig. 8 | FEL lasing with the EuPRAXIA witness. The plot reports the radiation growth along the undulator coordinate z . The inset shows the resulting radiation spectrum.